Mach reflection in axisymmetric internal supersonic flow

Tao Zhang,[1] Jianrui Cheng,[1] Haochen Xiong,[1] Ralf Deiterding,[2] Chongguang Shi,[1,*] Chengxiang Zhu,[1] and Yancheng You

[1]*School of Aerospace Engineering, Xiamen University, Xiamen, Fujian 361005, China*
[2]*School of Engineering, University of Southampton, Southampton SO16 7QF, United Kingdom*

(Received 3 November 2025; accepted 12 May 2026; published 12 June 2026)

Mach reflection (MR) of axisymmetric internal shocks in a steady supersonic flow is studied analytically and numerically in this paper. An analytical model, developed from a recent planar model and based on the curved shock theory and the method of curved shock characteristics, is utilized in the investigation. The presence of a center body as the unique geometry component in axisymmetric internal flow has been included. The comparison with numerical simulations shows that the primary flow configurations of axisymmetric internal shock MRs can be accurately predicted. By utilizing the analytical model, the shape of the slip line and the size of the Mach disk are studied. An in-depth analysis was conducted on the phenomenon where, at a specific wedge angle and with a sufficiently small outlet radius, the interference between the trailing-edge expansion fan and the slip line occurs downstream of the sonic throat, resulting in the size of the Mach disk being independent of the outlet radius. It is indicated that the formation of the sonic throat without relying on the trailing edge expansion fan is attributed to the negative pressure gradient that arises behind the reflection shock. Such pressure gradients are related to slip line deflection, with flatter slip lines implying greater negative pressure gradients being generated. Thus, the independent formation of the sonic throat is more feasible when the wedge angle is small enough, where the triple point is close to the von Neumann criterion and the deflection of the slip line is slight.

DOI: 10.1103/rbtm-hhcc

I. INTRODUCTION

Shock reflection is a fundamental phenomenon which exists widely in supersonic and hypersonic flows. Since Mach [1] experimentally observed two types of reflection configurations, known as regular reflection (RR) and Mach reflection (MR), the phenomenon has been extensively studied in terms of flow mechanisms and transition criteria [2]. The two configurations in steady supersonic flows are illustrated schematically in Fig. 1. The supersonic incoming flow M_0 is compressed by a wedge (w) with a deflection angle of δ_w, producing an incident shock wave (i) that exhibits a shock angle θ_i. For the RR configuration [Fig. 1(a)], the incident shock intersects the reflecting surface at point G, creating a reflected shock wave (r). In MR [Fig. 1(b)], the Mach stem (m), which is a strong shock, stands between the incident shock and the reflecting surface, with the foot perpendicular to the reflecting surface. The reflected shock is emitted from the intersection of the incident shock and the Mach stem and therefore, this point is commonly referred to as the triple point T. Since the flow velocity behind the reflected shock deviates from that downstream of the Mach stem, a slip line appears downstream of the triple point. At the trailing edge of the wedge, an expansion fan (e) forms in both configurations and interferes with the reflected shock.

*Contact author: chongguangshi@xmu.edu.cn

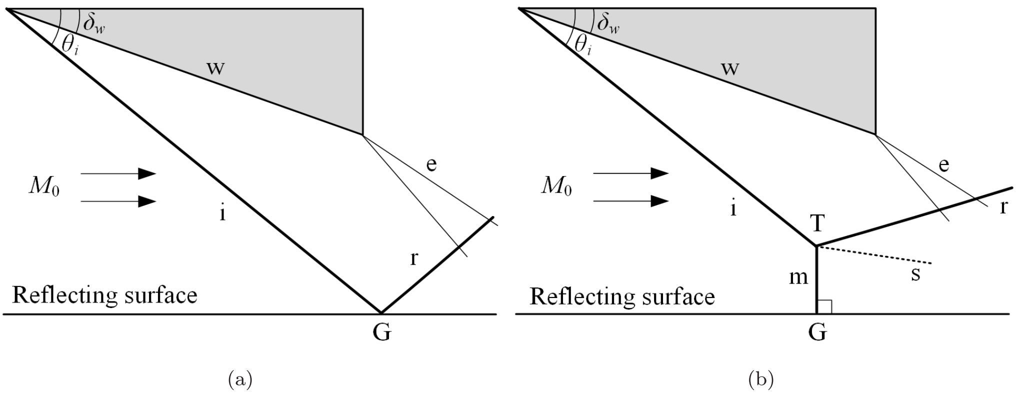

FIG. 1. Schematic illustration of (a) RR and (b) MR.

The transition criteria between RR and MR configurations have been discussed for several decades until von Neumann [3,4] proposed the mechanical equilibrium criterion (also referred to as the von Neumann criterion) and the detachment criterion. The von Neumann criterion establishes the minimum angle θ_N for the incident shock to theoretically result in MR, while the detachment criterion determines the maximum shock angle θ_D for RR to exist. Since θ_N is smaller than θ_D for the same M_0, a dual solution domain emerges between the two criteria. In the dual solution domain, both reflection configurations are possible, and their occurrence depends on the establishing history of the flow field [5–7]. Moreover, although RR and MR can remain stable within the dual solution domain, they can transition from one state to the other when a disturbance of a certain threshold level is applied [8–10].

As the most distinctive feature of the MR configuration, the size of the Mach stem has always been a major research subject. Over the years, several analytical models have been developed to predict the Mach stem height in steady flows with increasing accuracy. Early works [11,12] modeled the flow behind the Mach stem as an isentropic quasi-one-dimensional converging nozzle, which is still widely used to this day. Furthermore,they assumed sonic flow occurs at the throat, positioned where the leading expansion wave intersects a linear slip line, with subsonic flow accelerating to sonic speed there. To address the limitations of this assumption, Li and Ben-Dor [13] made some improvements in subsequent research by considering the interactions of the reflected shock and the slip line with the expansion fan. Their analytic model accounts for slight curvature in the reflected shock, the slip line, and the Mach stem, and allows the sonic throat to occur downstream of the leading expansion wave. Since then, further research has been conducted to refine the modeling [14–16] and extend it to more complex flows [17–20].

Despite some efforts to extend the use of analytical models to relatively complex flow scenarios, the studies mentioned above are still restricted to planar flows. In recent times, there has been a growing interest in axisymmetric internal flows [21,22], particularly with the advancement of three-dimensional inward-turning inlets [23,24]. Early work showed that axisymmetric internal shocks intensify toward the symmetry axis due to intrinsic effects of flow convergence [25–27]. The shock angles have been proven to inevitably exceed the detachment criterion, leading to an MR structure [28,29]. This shock intensification and convergence cause nonuniform flow behind the incident shock. Moreover, it has been observed that in axisymmetric shock MRs, the sonic throat can occur upstream of the expansion fan when the wedge angle is small [30]. These relatively complex flow regimes present a challenge for flow field modeling and analysis of associated flow features. Ferri [31] used the method of characteristics (MOC) to predict supersonic flow downstream of axisymmetric shocks, estimating the subsonic region size by extrapolating the shock geometry. Isakova *et al.* [32] developed a nonlinear theory to investigate weak incident shock amplification and estimate the Mach-disk radius based on free stream Mach number and

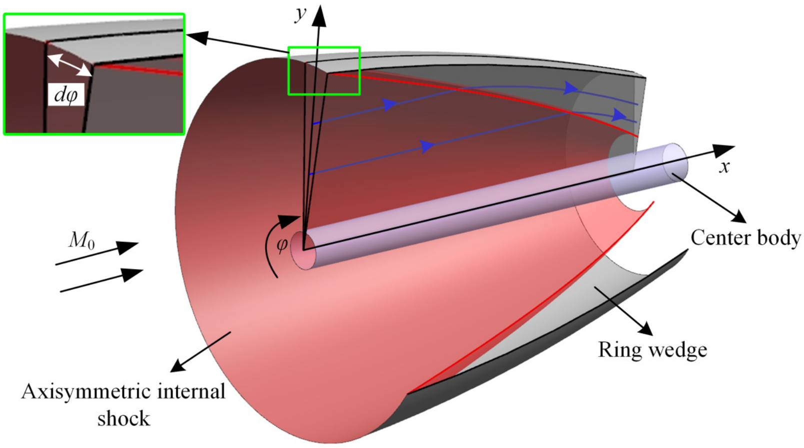

FIG. 2. Schematic diagram of a supersonic axisymmetric internal flow.

wedge angle. However, this estimation approach may have limitations as it does not account for the influence of downstream flow. Shoesmith and Timofeev [33] investigated via numerical simulations the hysteresis phenomenon in shock reflection structures with varying center body. Subsequently, they [34] created an axisymmetric MR model using MOC and a quasi-one-dimensional flow assumption, studying the expansion fan's effect on MR configurations. Nevertheless, their model did not account for the presence of a center body, nor explore the fundamental mechanism governing the formation of a sonic throat independently of the expansion fan. In their most recent work [35], they further extended this model to include a center body and, using this model together with numerical simulations, explored the hysteresis behavior of RR and MR as the center-body height varies.

Building on previous work, this paper extends the analytical model for planar shock MRs of Zhang *et al.* [19] to axisymmetric internal flows. The model also incorporates a center body to investigate the detailed flow structures, with a primary focus on revealing the formation mechanism of a sonic throat that can occur independently of the trailing-edge expansion fan, along with other flow features such as the slip line shape and Mach disk size. The analytical model and numerical methods of computational fluid dynamics (CFD) are introduced in Sec. II. In Sec. III, model predictions are compared with numerical simulations and then applied to analyze these flow features. Finally, conclusions are summarized in Sec. IV.

II. ANALYTICAL MODEL AND NUMERICAL METHODS FOR AXISYMMETRIC INTERNAL SHOCK MRS

This section begins by examining the distinct features of supersonic axisymmetric internal flows and their associated shock reflection phenomena (Sec. II A). In response to these new features, we present an analytical model suitable for axisymmetric internal shock MRs in Sec. II B. The proposed model is extended from the model of Zhang *et al.* [19] for planar curved shock MRs. Then the numerical methods utilized in this study are introduced in Sec. II C, along with a grid convergence analysis. Throughout this paper, p, ρ, V, M, δ, θ, and γ denote the pressure, density, velocity, Mach number, flow deflection angle, shock angle, and specific heat ratio of the gas, respectively.

A. Overall features of axisymmetric internal flow

Figure 2 schematically displays the geometry of a supersonic axisymmetric internal flow induced by a ring wedge, which is shaded in gray. The three-dimensional view is intended to illustrate the flow patterns of axisymmetric flow, with only the incident shock (the red surface) depicted to promote clarity. The shock configurations related to reflection will be presented in a two-dimensional view in Sec. II B. In the figure, the x, y, and φ axes denote the directions of axial, radial and circumferential, respectively. $d\varphi$ represents a circumferential differential element, and the blue lines within the element depict the streamlines. As observed, in axisymmetric flows, circumferential compression arises from geometric continuity requirements. As a fluid element approaches the symmetry axis along radially converging streamlines (Fig. 2), its fan-shaped appearance results from the azimuthal narrowing of the flow channel—where the same angular width ($d\varphi$) spans a smaller arc length ($ds = rd\varphi$) as radius r decreases. This compresses the element kinematically, as mandated by mass conservation [36,37]. Conversely, radial divergence causes circumferential expansion.

In axisymmetric internal flows, the incident shock will deflect the free stream toward the axis of symmetry. Consequently, a circumferential compression occurs along the streamline behind the incident shock, leading to a pressure increase and the generation of the so-called convergence effect. This convergence effect results in some distinct features of axisymmetric shock MRs compared to planar ones. First, the incident shocks in axisymmetric flows continuously intensify as they develop downstream, with the post-incident shock flows displaying significant nonuniformity even when the wedge is straight in the flow plane. This complexity of the flow fields is greater than that of planar flows, wherein a straight wedge produces a linear incident shock followed by a uniform flow field. The nonuniformity of axisymmetric flows may be the fundamental reason that the sonic throat can form without relying on the presence of the trailing-edge expansion fan. Second, due to the convergence effect, MR inevitably occurs over the axis of symmetry for axisymmetric internal shocks [28,29]. Therefore, in the design of axisymmetric internal flows, a cylindrical center body aligned along the axis is often used to prevent shocks from converging on the axis. A typical example is the basic flow field of an inward-turning inlet [24]. Without this design feature, the resulting Mach stem can cause considerable total-pressure loss and extensive subsonic flow, which reduces the compression efficiency of the flow field and may even lead to flow instability. Considering that the convergence effect is influenced by the distance to the symmetry axis, the radius of the center body must be regarded as an independent variable. This fact also contributes to the differences between axisymmetric and planar flows, as in planar flows, the lifting of the reflecting surface can be equivalent to a reduction in the area of the outlet (or an increase in the length of the wedge).

Despite the presence of circumferential compression, the axisymmetric flow remains two-dimensional within each flow plane (i.e., the x-y plane). Therefore, for the rest of this paper, all of the analysis and calculations will be conducted in the x-y plane, based on the two-dimensional Euler equations.

B. Modeling for axisymmetric internal shock MRs

This subsection will detail the analytical modeling approach for axisymmetric internal shock MRs. Figure 3(a) presents a schematic illustration of the shock configurations on the x-y plane. In the diagram, the axis of symmetry is denoted by the dash-dotted line, and the shaded area above it represents the center body. The compression surface of the ring wedge (w), in this paper, is straight within the flow plane and features a compression angle of δ_w. The inlet radius R_0 is defined as the distance from the leading edge of the wedge to the symmetry axis, and the outlet radius R_e as the distance from the trailing edge to the axis. The radius of the center body is R_c.

As illustrated, the axisymmetric internal MR flowfield contains components analogous to planar cases: incident shock (i), reflected shock (r), Mach disk (m), slipline (s), and expansion fan (e). The shocks and slipline that intersect at the triple point (T) divide the flow field into four regions [regions (0)–(3)]. While regions (1) and (2) remain supersonic, region (3) downstream of the Mach disk acts as a de Laval nozzle, accelerating flow from subsonic to supersonic through the converging-diverging slipline. The horizontal point of the slipline defines the sonic throat (t), with its radius R_t

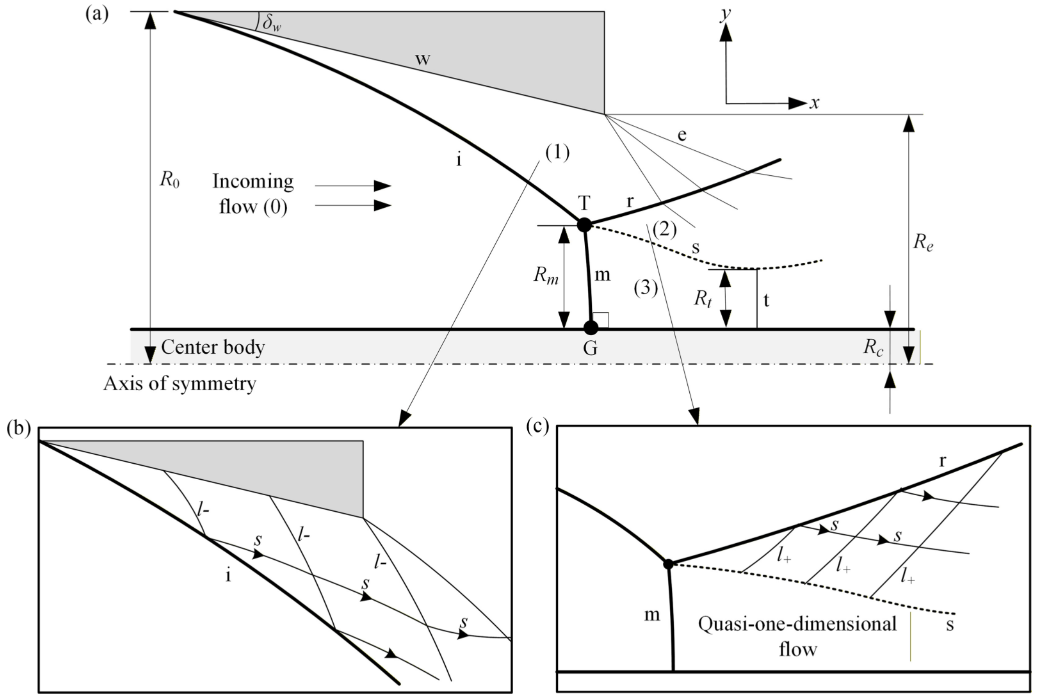

FIG. 3. (a) Schematic illustration of axisymmetric internal shock MRs on the x-y plane; (b) and (c) solution approaches for different regions in the flow field based on the MOCC.

being the minimum distance to the reflecting surface. The distance from the triple point T to the reflecting surface is denoted as the Mach-disk radius R_m.

Axisymmetric internal conical shocks typically exhibit complex bi-directional curvature, resulting in highly nonuniform postshock flows. To address these challenges in solving the supersonic flow field, the curved shock theory (CST) described by Mölder [38] and the method of curved shock characteristics (MOCC) of Shi *et al.* [39] were employed, as established in our prior work [19]. CST establishes the relationship between shock curvatures and the flow gradients across the shock. MOCC utilizes post-shock flow gradients to solve the downstream supersonic flow field along streamlines and characteristics. Notably, the solution in region (2) is coupled with the quasi-one-dimensional isentropic flow equations in region (3), as both share the slip line as a common boundary. The remainder of this subsection will detail the solution methodology for each region.

First, Fig. 3(b) presents a schematic of the MOCC applied to the incident shock and the flow region (1) behind it. The thick line represents the incident shock wave (i), and the thin line represents the streamlines (s) and the right-running characteristics (l-). The expansion wave at the trailing edge point aligns with the right-running characteristics emitted from that point. In the calculation, the flow parameters upstream and downstream of the incident shock satisfy the classical shock relations. Based on this, Mölder [38] derived the relationship between the flow gradients upstream (subscript 0) and downstream (subscript 1) of the shock by differentiating these shock relations, known as the curved shock equations,

$$\begin{aligned} A_{0,i}P_0 + B_{0,i}D_0 + E_{0,i}\Gamma_0 &= A_{1,i}P_1 + B_{1,i}D_1 + C_iS_{a,i} + G_iS_{b,i}, \\ A'_{0,i}P_0 + B'_{0,i}D_0 + E'_{0,i}\Gamma_0 &= A'_{1,i}P_1 + B'_{1,i}D_1 + C'_iS_{a,i} + G'_iS_{b,i}, \\ A''_{0,i}P_0 + B''_{0,i}D_0 + E''_{0,i}\Gamma_0 &= A''_{1,i}P_1 + B''_{1,i}D_1 + E''_{1,i}\Gamma_1 + C''_iS_{a,i} + G''_iS_{b,i}. \end{aligned} \tag{1}$$

where P, D, and Γ represent the normalized pressure gradient, streamline curvature, and normalized vorticity,

$$P = \frac{\partial p/\partial s}{\rho V^2}, \quad D = \partial\delta/\partial s, \quad \Gamma = \omega/V. \tag{2}$$

S_a and S_b are shock curvatures in the flow plane and flow-normal planes, respectively. Specifically, S_a is defined as the derivative of the shock inclination angle along the shock, $\partial\theta_1/\partial\sigma$. In axisymmetric flows, S_b is given by $-\cos\theta/y$, a quantity that increases as the shock approaches the axis. In planar flows, S_b is identically zero. The coefficients A, B, E, C, and G are dependent on the flow parameters provided by shock relations and can be found in [38]. The curved shock equations allow for the calculation of the post-shock flow gradients P_1, D_1, and Γ_1 once the free stream conditions and shock geometry are determined. These gradients reveal the convergence/divergence of flow, but only tenable within close proximity to the shock. The propagation of disturbances along the characteristics enables the analysis of the flow field further downstream. At every point in a supersonic flow, three characteristic directions exist: the characteristics l_+ and l_-, along with the streamline s. To obtain the flow parameters away from the shock, Shi *et al.* [39] derived the following MOCC equations along characteristics and streamlines,

$$\begin{aligned}
&\frac{\mathrm{d}p}{\mathrm{d}l_\pm} - \rho V^2(P\cos\mu \mp D\sin\mu) = 0, \quad \frac{\mathrm{d}\delta}{\mathrm{d}l_\pm} - \frac{D\sin\mu \mp P\cos\mu}{\tan\mu} \pm j\frac{\sin\delta\sin\mu}{y} = 0,\\
&\frac{\mathrm{d}p}{\mathrm{d}s} - \rho V^2 P = 0, \quad \frac{\mathrm{d}\delta}{\mathrm{d}s} - D = 0, \quad \rho V\frac{\mathrm{d}V}{\mathrm{d}s} + \frac{\mathrm{d}p}{\mathrm{d}s} = 0, \quad \frac{\mathrm{d}p}{\mathrm{d}s} - \frac{\gamma p}{\rho}\frac{\mathrm{d}\rho}{\mathrm{d}s} = 0.
\end{aligned} \tag{3}$$

In the equations, μ refers to the Mach angle $\arcsin(1/M)$, which represents the angle between the streamline and characteristics. The variable j takes on the value of 0 in planar flow and 1 in axisymmetric flow. Compared to the general method of characteristics, MOCC simplifies the iteration procedure by utilizing just one characteristic line and one streamline to solve the equations. For the internal flow, the equations are solved in the streamline and right-running characteristic (s, l_-) coordinates, as shown in Fig. 3(b).

Following the same approach, the flow parameters and gradients downstream of the reflected shock and the Mach stem can be determined using the curved-shock equations. This then allows the flow fields in regions (2) and (3) to be resolved. As illustrated in Fig. 3(c), regions (2) and (3) are separated by a slip line, which is essentially a streamline passing through the triple point. Therefore, region (3) is basically an annular stream tube enclosed by the surface of the center body and the slip line, and can effectively be considered a quasi-one-dimensional isentropic flow. Once the cross-sectional area of the stream tube is determined, the flow Mach number and pressure at the corresponding cross-section can be obtained according to the following one-dimensional isentropic flow equation,

$$\frac{A}{A_m} = \frac{M_m}{M}\left\{\frac{1+[(\gamma-1)/2]M^2}{1+[(\gamma-1)/2]M_m^2}\right\}^{(\gamma+1)/2(\gamma-1)}, \quad \frac{p}{p_m} = \left\{\frac{1+[(\gamma-1)/2]M^2}{1+[(\gamma-1)/2]M_m^2}\right\}^{1/(\gamma-1)}. \tag{4}$$

Here, M_m and p_m are the average Mach number and pressure immediately downstream of the Mach stem and can be calculated by performing a weighted integration based on the local mass flow rate. The shape of the Mach stem is modelled as a fourth-order polynomial using Taylor series expansion, which is based on its inclination angle and curvature at the triple point T, as well as features perpendicular to the reflecting surface at the foot G [40]. A_m represents the projection area of the Mach disk in the direction of the incoming flow, while A represents the cross-sectional area of the stream tube. These two areas can be calculated using the following formulas, respectively,

$$A_m = \pi\left[(R_m + R_c)^2 - R_c^2\right], \quad A = \pi\left(y_s^2 - R_c^2\right), \tag{5}$$

where y_s represents the y coordinate of a point on the slip line. According to Eqs. (4) and (5), once the coordinates of a point on the slip line are known, the corresponding pressure can be determined.

Hence, the slip line can be regarded as a "soft boundary" with a given pressure distribution. With the known pressure distribution and flow parameters of region (1), the MOCC can be applied to solve for the reflected shock wave and the corresponding post-shock flow field (region 2), which is an external flow with a nonuniform incoming flow. Therefore, the MOCC equations (3) are solved in the streamline and left-running characteristic (s, l_+) coordinates, as shown in Fig. 3(c).

The above process describe the solution approach for the entire MR flow field on the premise that the triple point position (or the Mach-disk radius) is clear. Nevertheless, in practice, the location of the triple point T is initially unknown and may occur at any position on the incident shock, as long as the local shock angle θ_i is greater than the von Neumann criterion θ_N. For planar concave incident shock, the triple point can even appear where the shock angle is less than θ_N, as inverse MRs are possible [19]. Therefore, the upcoming objective is to determine the Mach-disk radius, using the sonic throat criterion as the basis for computation. To perform the calculation, the first step is to assume an initial radius R_m^* for the Mach disk, from which an initial position for the triple point is obtained. Following from this, the flow parameters for the complete flow field, as well as the shape of the slip line, can be derived using the CST and MOCC. Meanwhile, the projected area A_m^* of the Mach disk can be determined by Eq. (2) with the estimated Mach-disk radius R_m^*. Then, the corresponding sonic throat area A_t^* can be calculated by utilizing the following one-dimensional isentropic flow equation,

$$\frac{A_m^*}{A_t^*} = \frac{1}{\overline{M}_m}\left(1 + \frac{\gamma - 1}{2}\overline{M}_m^2\right)^{(\gamma+1)/2(\gamma-1)}. \tag{6}$$

where $\overline{M}_m$ represents the average Mach number immediately behind the Mach disk. Typically, the sonic throat appears at the narrowest section of the flow passage, which is located at the lowest point of the slip line. Therefore, the next step involves verifying whether the minimum area between the slip line and the center body is equal to A_t^*. If it is not, then the value of R_m^* should be adjusted, and the entire set of steps detailed above must be reiterated until a converged R_m^* value is achieved.

The process described above is applicable not only to internal axisymmetric shock MRs induced by wedges with straight generatrixes but also to the cases with curved generatrixes. However, since this paper primary examines the impact of circumferential compression on the flow configurations, the following analyses are conducted with straight wedges as examples to increase concision.

C. Numerical methods and grid convergence analysis

The numerical simulations carried out in this paper are conducted using the open-source program AMROC (Adaptive Mesh Refinement in Object-Oriented C++ [41]) [42,43], which improves the calculation efficiency with a high grid resolution. The axisymmetric two-dimensional Euler equations for an ideal gas are solved using the finite-volume approach. The air is assumed to be a calorically perfect gas with a constant specific heat ratio γ of 1.4. A hybrid Roe-HLL Riemann solver and dimensional splitting are utilized to calculate the convective fluxes. To prevent the carbuncle phenomenon intrinsic to Roe schemes, a multi-dimensional entropy correction is employed [44]. A second-order-accurate Runge-Kutta scheme is used to integrate the additional terms arising from axial symmetry as right-hand side sources in a Strang splitting approach. The MUSCL-Hancock approach with Minmod-limiter in conservative variables is applied to obtain a method of overall second order accuracy [42].

Figure 4 illustrates the computational domain and the boundary conditions used in the simulations. The dash-dotted line represents the centerline of rotation of the axisymmetric flow field. The upper surface of the center body, which functions as the reflecting surface, is the lower boundary of the computational domain. The key geometric parameters of the model, including the wedge angle δ_w, inlet radius R_0, outlet radius R_e, and center body radius R_c, are indicated in the figure for clarity. In the calculations, a supersonic inflow condition is applied to the left boundary, where a free stream Mach number M_0 is specified. The slip boundary condition is used on the upper boundary and the lower boundary. The outflow boundary is extrapolated from the interior under the assumption that

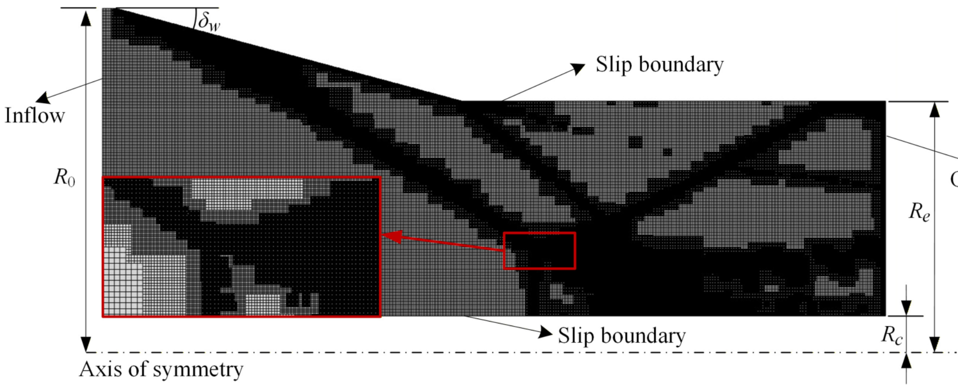

FIG. 4. Computational domain and boundary conditions, as well as the adaptive mesh refinement for the calculation of axisymmetric internal shock MR using AMROC.

the derivatives of all flow parameters are zero. For a precise simulation outcome, this paper utilizes a refined mesh, to which three levels of adaptive mesh refinement by a factor of 2 are applied. The adaptive mesh refinement for the calculation of axisymmetric internal shock reflection using AMROC is also illustrated in Fig. 4. The mesh near the triple point is enlarged for clarity. The grid adaptation is triggered by a discontinuity detector, similar to the Minmod-limiter function, that is applied in pressure only.

To verify the grid resolution, a representative case ($M_0 = 4$, $\delta_w = 15^\circ$, $R_e/R_0 = 0.7$, $R_c/R_0 = 0$) was simulated with two different grid scales (750×300 and 1500×600), as shown in Fig. 5. In the simulations, the Courant-Friedrichs-Lewy (CFL) number was set to 0.7. The computation was conducted for a total nondimensional time of $t = 14.95R_0/a_0$ to ensure the convergence, with results at $t = 8.97R_0/a_0$ are included to demonstrate the sufficiency of this computational time. It is observed that although localized flow oscillations (e.g., those near the slip line) can not fully converge in this unsteady simulation, the main shock structures have reached a steady state. This is further supported by Fig. 6, which shows the convergence of the normalized Mach-disk radius over time. It can be observed that as the computation proceeds, the Mach-disk radius gradually stabilizes,

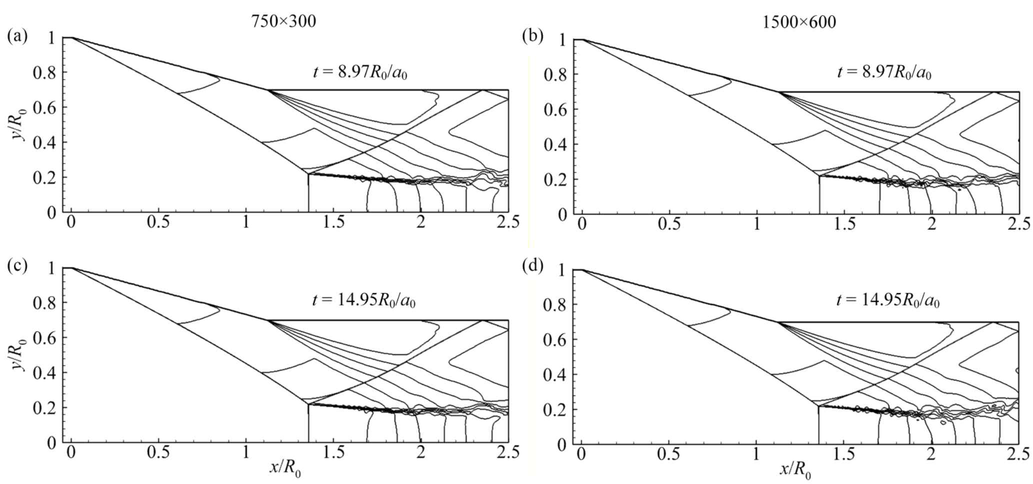

FIG. 5. Mach number contours obtained with two grid resolutions and different computational times for the case of $M_0 = 4$, $\delta_w = 15^\circ$, $R_e/R_0 = 0.7$, $R_c/R_0 = 0$.

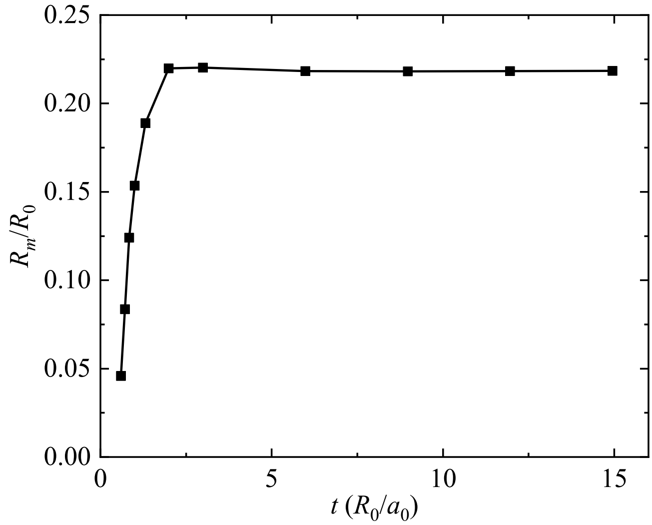

FIG. 6. Convergence of the normalized Mach-disk radius in the simulation for the case of $M_0 = 4$, $\delta_w = 15^\circ$, $R_e/R_0 = 0.7$, $R_c/R_0 = 0$.

confirming that a steady state has been reached. Furthermore, the primary flow structures are similar and well-captured by both grids, albeit with slight differences in flow details. The Mach-disk radii computed with the two grids are 0.2184 and 0.2186, with a relative difference of less than 0.5%. These results demonstrate that the mesh density of 750 × 300 is accurate enough for simulations and is consequently utilized throughout this paper.

III. RESULTS AND DISCUSSION

This section initially compares the flow configurations obtained from the analytical model presented in Sec. II to the CFD results. After that, analytical calculations and numerical simulations are combined to investigate the flow features. The formation mechanism of the sonic throat and the influence of the center body on flow structures are emphasized.

A. Flow configurations

We begin by examining the overall flow structures of axisymmetric MRs. Fig. 7 compares the analytical and numerical Mach number contours of the flow field for three cases (A–C), whose parameter configurations are listed in Table I. The black solid lines represent the numerical simulation results, while the red dashed lines correspond to the analytical calculation results. The analytically calculated sonic throat is indicated by a blue line, while the sonic line from numerical simulation is represented by green. In case A [Fig. 7(a)], the incident shock is reflected on the symmetry axis since the center body radius is 0. The considerable compression angle of the wedge

TABLE I. Parameter configurations for the three cases in Fig. 7.

Case no.	M_0	δ_w(deg.)	R_c/R_0	R_e/R_0
A	5	21	0	0.6
B	6	18	0.1	0.7
C	6	10.7	0	0.5

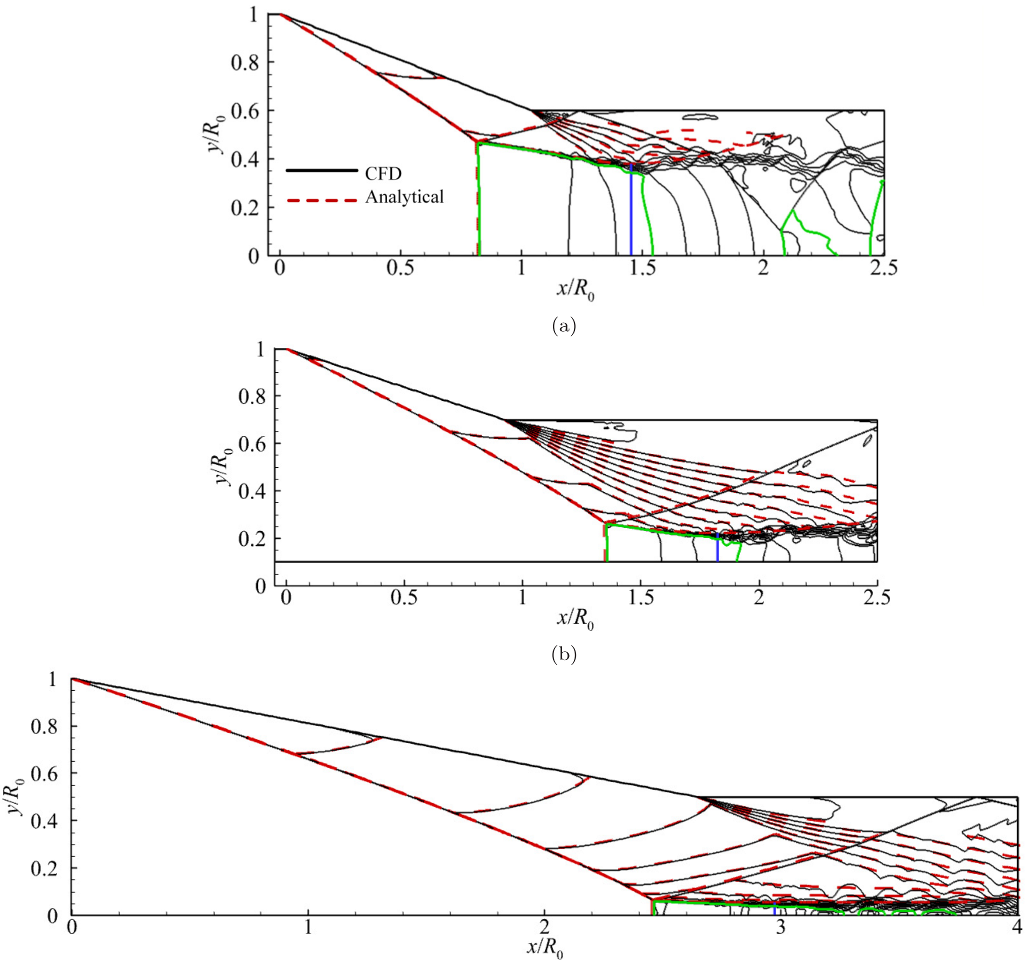

FIG. 7. Comparison of the analytical and numerical results: (a)–(c) correspond to cases A–C in Table I, respectively. The blue line denotes the analytical sonic throat, and the green lines represent the numerical sonic lines.

results in a relatively larger Mach disk with a radius nearly half that of the inlet radius. As a result of the upstream location of the triple point, the reflected shock is close to the trailing edge. If the Mach disk continues to increase, the reflected shock will impinge upon the wedge surface, making the flow field challenging to stabilize [13]. In case B [Fig. 7(b)], the center body radius R_c/R_0 has been increased to 0.1. The incident shock reflects over the surface of the center body and the triple point is close to the leading expansion wave from the trailing edge. In both of the above cases, the sonic throat occurs within the region influenced by the expansion fan, as expansion waves can promote the formation of the throat. However, in case C [Fig. 7(c)], the sonic throat occurs ahead of the expansion fan. This shows that in axisymmetric flow, the formation of a sonic throat can occur independently of the expansion fan under certain conditions. Moreover, as observed in Figs. 7(a)–7(c), the discrepancy between the sonic throat location predicted by the analytical model and that obtained from numerical simulations increases as the Mach disk size decreases. This occurs mainly because when the Mach disk is small, the variation in slip-line angle along the flow path is also minor, making the sonic throat position more sensitive to small changes. Consequently, even a slight deviation in the Mach stem height can lead to a noticeable shift in the sonic throat location.

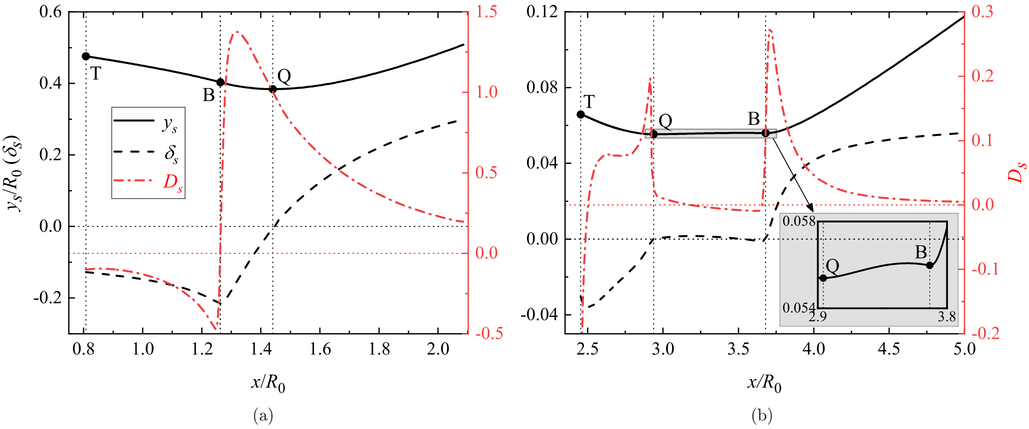

FIG. 8. Slope and curvature of the analytical slip line: (a) case A; (b) case C. Here, T denotes the triple point, B is the intersection point of the first trailing-edge expansion wave with the slip line, and Q marks the point where the slip line turns horizontal, indicating the location of the sonic throat.

To clarify the unique spatial relationship between the trailing-edge expansion fan and the sonic throat in case C, Fig. 8 presents the analytical geometry of the slip line, where y_s denotes the vertical coordinate, δ_s the inclination angle, and D_s the curvature. The intersection between the slip line and the first transmitted expansion wave is denoted as point B, while where the slip line becomes horizontal (i.e., the sonic throat) is identified as point Q. The initial curvature of the slip line at the triple point is negative. For case A, the curvature of the slip line remains negative until it interferes with the expansion fan at point B, where the curvature undergoes a sudden increase to a positive value, with the inclination angle beginning to rise rapidly. Under the influence of the expansion fan, the slip line gradually deflects horizontally at point Q, where the inclination angle becomes zero. At this particular location, the flow area between the slip line and the center body (or the axis) is minimal, leading to a throat where the flow velocity is sonic. In both cases A and B, point P is located downstream from point B. However, it is noteworthy that, in case C [Fig. 8(b)], the sonic throat is formed before the expansion fan interferes with the slip line, leading to point P being upstream of point B. In this scenario, the curvature increases rapidly to a positive value well before the slip line intersects the transmitted expansion fan. This may be attributed to expansion occurring downstream of the reflected shock in axisymmetric internal flows (see Sec. III C for detailed analysis). Behind point Q, the slip line remains stable until it encounters the first expansion wave at point B, after which it experiences a rapid upward deflection. The flow between points Q and B is supersonic, which means that the expansion fan cannot affect the formation of the sonic throat under this condition. Furthermore, it is worth noting that the slip line undergoes slight fluctuations between points P and B, initially rising before decreasing. It is conceivable that should the expansion waves continue to move downstream, the slip line may continue to descend, giving rise to the formation of a second subsonic pocket and potentially additional sonic throats, as observed by Ji *et al.* [30].

B. Mach-disk radius

Given that the size of the Mach disk is one of the most critical parameters in MRs, it requires special attention. Table II provides a quantitative comparison between the analytical and numerical normalized Mach-disk radii R_m/R_0 under various freestream and geometric conditions. It can be observed that the Mach-disk radius predicted by analytical calculations is slightly larger than that measured from numerical results. Given that the incident shock and the post-shock flow field calculated by the analytical model are nearly identical to those obtained from CFD simulations

TABLE II. Mach-disk radii for various conditions.

Case no.	Conditions				R_m/R_0	
	M_0	δ_w (deg.)	R_c/R_0	R_e/R_0	CFD	Analytical
1	3	15	0	0.7	0.306	0.310
2	4	15	0	0.7	0.219	0.223
3	5	21	0	0.7	0.370	0.376
4	5	21	0	0.6	0.467	0.476
5	6	18	0.1	0.7	0.160	0.167
6	6	18	0.3	0.7	0.065	0.073
7	6	10.7	0	0.6	0.061	0.066
8	6	10.7	0	0.5	0.061	0.066

(as shown in Fig. 7), the discrepancy in Mach-disk size may be attributed to the one-dimensional flow assumption and the fluctuations of the slip line. Nevertheless, the adequacy of the analytical calculation is overall acceptable and can reveal the influence of the freestream and geometric parameters on the size of the Mach disk. Notably, in cases 7 and 8, the Mach-disk radius remains unchanged, despite the variation in outlet radius R_e/R_0 (changing from 0.6 to 0.5). This phenomenon is a direct result of the sonic throat forming upstream of the trailing-edge expansion fan, as noted by Ji *et al.* [30], meaning that the area affected by the expansion fan is separated from the throat by a supersonic flow region. Consequently, the formation of the Mach disk and sonic throat are not influenced by the position of the trailing edge under these circumstances. In contrast, cases 3 and 4 demonstrate a significant influence of the outlet radius on the Mach-disk size. This occurs because the first expansion wave that originates from the trailing edge hits the slip line before the sonic throat, and therefore the expansion fan can impact the size of the Mach disk by facilitating the formation of the throat.

Figure 9 further compares the Mach disk heights predicted by our analytical model with those from the earlier work of Shoesmith and Timofeev [34], including both their analytical and numerical results. The abscissa θ_w in the figure is the initial incident shock angle, while the other parameters

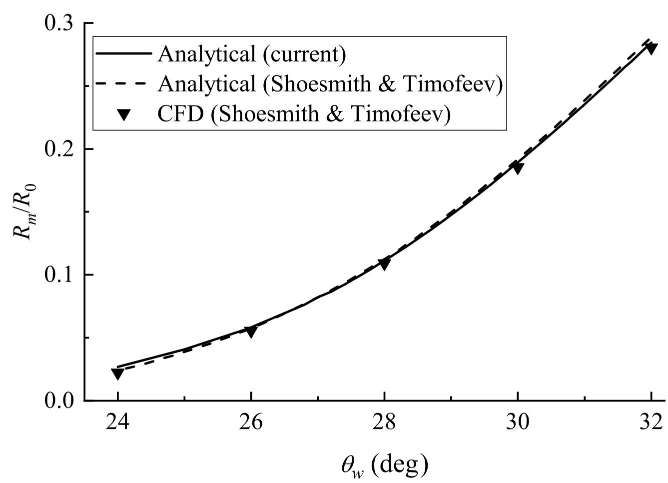

FIG. 9. Comparison of Mach disk sizes predicted by our analytical model and the Shoesmith and Timofeev model [34] with their numerical simulation results, for $M_0 = 3$, $l_w/R_0 = 1$, $R_c/R_0 = 0$. The abscissa θ_w denotes the initial incident shock angle.

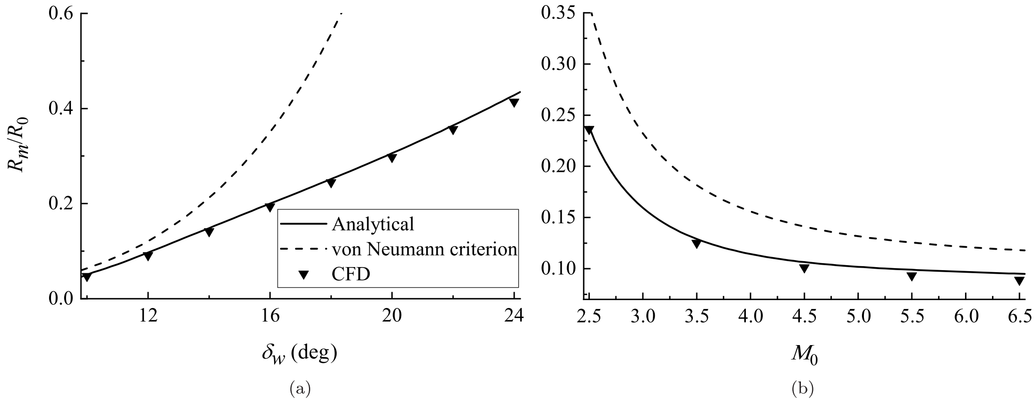

FIG. 10. Comparisons of the analytical Mach-disk radius with the numerical results for (a) varying wedge angle δ_w at $M_0 = 6$, $R_c/R_0 = 0$, $R_e/R_0 = 0.7$; and (b) varying free stream Mach number M_0 at $\delta_w = 12^\circ$, $R_c/R_0 = 0$, and $R_e/R_0 = 0.7$.

are fixed at $M_0 = 3$, $l_w/R_0 = 1$, and $R_c/R_0 = 0$, where l_w denotes the length of the ring wedge. It can be seen that the predictions of our analytical model are highly consistent with those of Shoesmith and Timofeev, showing only minor discrepancies, and both are slightly higher than the numerical simulation results. For larger Mach disk sizes, our predictions are slightly lower than those of Shoesmith and Timofeev and closer to the numerical results. For smaller Mach disk sizes, however, our predictions are slightly higher than theirs, resulting in a larger deviation from the numerical simulations. These results further validate the accuracy of the present analytical model across a wide range of incident shock angles.

Figures 10 and 11 provide a comparative analysis of the analytical Mach-disk radii and the CFD results for axisymmetric shock MRs under a broader range of conditions. Figure 10 compares the analytical Mach-disk radius with the numerical results for varying wedge angle δ_w and free stream Mach number M_0. The y coordinates of the points determined by the von Neumann criterion on the incident shock are also plotted in the figure as dashed lines. Figure 10(a) exhibits results with fixed conditions of $M_0 = 6$, $R_c/R_0 = 0$, and $R_e/R_0 = 0.7$, while Fig. 10(b) displays outcomes with $\delta_w = 12^\circ$, $R_c/R_0 = 0$, and $R_e/R_0 = 0.7$. The predictive results appear to be in good agreement with the numerical simulation. Both the predictive and numerical results are lower than the position

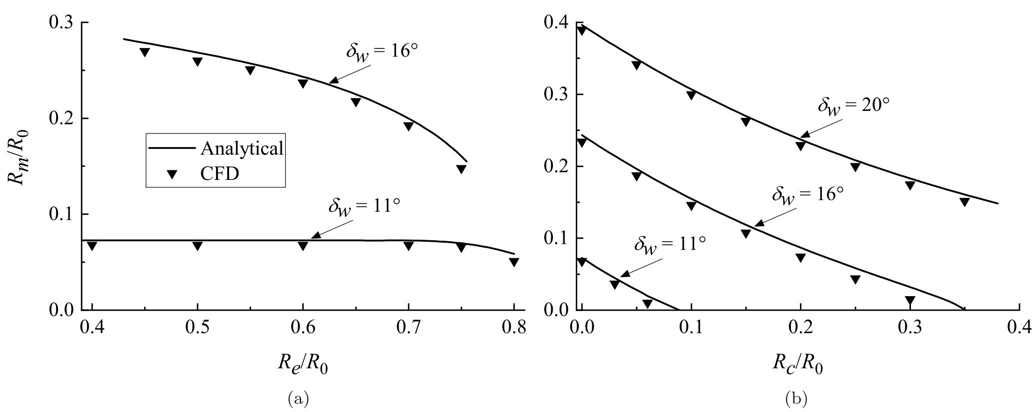

FIG. 11. Comparisons of the analytical Mach-disk radii with the numerical results for (a) $\delta_w = 11^\circ$ and 16° at $M_0 = 6$, $R_c/R_0 = 0$; (b) $\delta_w = 11^\circ$, 16° and 20° at $M_0 = 6$, $R_e/R_0 = 0.6$.

determined by the von Neumann criterion and exhibit an increasing departure as the wedge angle increases and the freestream Mach number decreases. Figure 10(a) reveals that the Mach disk radius experiences an almost linear growth as the wedge angle increases. This linear trend may not hold as the wedge angle decreases further as the Mach disk disappears only when the incident shock becomes a Mach wave, where $\delta_w = 0^\circ$ [29]. Unfortunately, when the wedge angle is small enough ($\delta_w < 10^\circ$ for $M_0 = 6$), the size of the Mach disk is too small, posing difficulties in applying the analytical model due to the high flow gradients near the axis. Despite this, we observe that as the wedge angle decreases, the position of the Mach disk rapidly approaches the location corresponding to the von Neumann criterion. Hence, in such scenarios, it may be appropriate to estimate the Mach disk size by using the von Neumann criterion, even though it could be slightly higher than the actual value. Figure 10(b) illustrates that the Mach disk decreases with increased free stream Mach number. The size of the Mach disk undergoes a rapid variation when the Mach number is low, whereas, for higher Mach numbers, the radius displays a more gradual change.

Figure 11 displays a comparison between the analytical Mach disk radius and the numerical simulations concerning different values of outlet radius R_e/R_0 and center body radius R_c/R_0. In Fig. 11(a), the wedge angles δ_w are fixed at 11° and 16°, respectively, while the free stream Mach number is fixed at 6, and the center body radius remains zero. It can be noticed that the Mach disk size displays distinctive trends concerning the outlet radius under the two different wedge angles. When the wedge angle is fixed at 11°, the Mach-disk radius undergoes negligible variations for small outlet radii since the interaction between the trailing edge expansion fan and the slip line occurs downstream the sonic throat. With an increase in outlet radius to a certain extent (about 0.7 to 0.75), the expansion fan moves upstream, and the intersection point between the first expansion wave and the slip line appears in front of the throat. In this situation, the presence of the expansion fan can facilitate the formation of the throat, resulting in a decrease in the Mach-disk size. In contrast, a fixed wedge angle of 16° leads to a Mach-disk size that consistently varies with the changes in outlet radius. Even with a further reduction in the outlet radius, the size of the Mach disk would not remain constant. Instead, such a reduction would result in an unstable MR configuration due to the impingement of the reflection shock on the wedge surface. This suggests that the sonic throat cannot be formed without the trailing edge expansion fan under the condition. Furthermore, for $\delta_w = 16^\circ$, the maximum outlet radius is more restricted to prevent the trailing edge expansion fan from impacting the incident shock wave, compared to $\delta_w = 11^\circ$.

Figure 11(b) presents results for wedge angles $\delta_w = 11^\circ$, 16°, and 20° at Mach 6, with fixed outlet radius $0.6R_0$. As the central body size increases, the Mach disk radius progressively decreases despite upstream movement of the triple point. At $\delta_w = 11^\circ$ and 16°, the Mach disk vanishes when the central body radius reaches approximately $0.09R_0$ and $0.35R_0$, respectively, indicating transition to RR. The phenomenon arises due to the gradual reduction in the intensity of the incident shock at the reflection point with an increase in the distance from the symmetry axis. When the strength of the incident shock falls below the von Neumann criterion, the MR configuration can no longer occur. For $\delta_w = 20^\circ$, however, the MR structure persists longer because the position satisfying the von Neumann criterion is located farther from the axis. Before the center body can expand to reach that point, the flow will be choked due to the high contraction ratio.

According to Li and Ben-Dor [13], choking initiates when the reflected shock impinges on the wedge surface. Based on this criterion, we derived the minimum outlet radius $R_{e,\min}$ required for flow establishment under $M_0 = 3$ and $M_0 = 6$ conditions (Fig. 12). The solid curve corresponds to zero center body radius ($R_c = 0$), where $R_{e,\min}$ first decreases then increases with wedge angle for both Mach numbers. Dashed and dash-dotted curves represent center body heights of 0.2 and 0.3, respectively. These curves exhibit left truncation boundaries because Mach reflection fails to form at small wedge angles. Significantly, increasing center body height raises $R_{e,\min}$—attributed to the elevated y coordinate of the triple point. This forward-shifted reflection position causes earlier shock impingement on the wedge, inducing choking at larger outlet radii. Therefore, the $R_{e,\min}$ boundary establishes a critical design criterion for supersonic inlets by defining the minimum allowable throat area to prevent unstart.

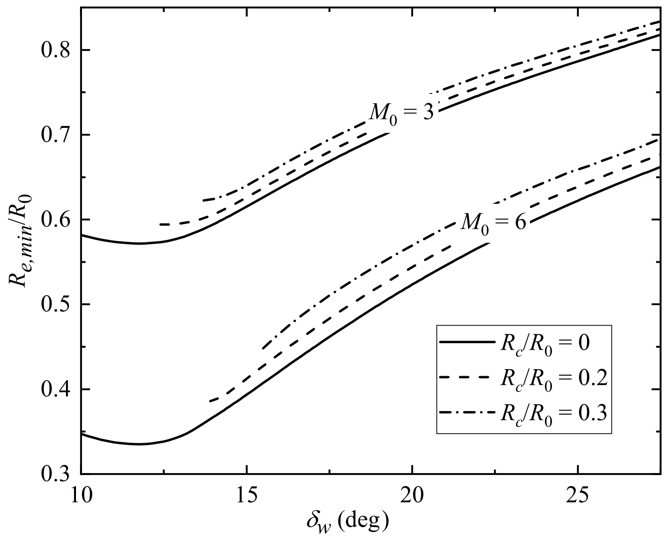

FIG. 12. Normalized lower limiting values of R_e/R_0 for the reflected shock not to impinge the wedge surface at $M_0 = 3$ and $M_0 = 6$.

C. Formation mechanism of the sonic throat

This section delves into the formation mechanism of the sonic throat below the slip line, with particular emphasis on the conditions and factors that allow the throat to occur independently of the trailing edge expansion fan in axisymmetric internal flows. In MRs, the shape of the slip line is governed primarily by its interaction with the characteristics [13,15], which are physically the expansion and compression waves in the flow field. Defining the strength of a characteristic as the pressure gradient taken along the direction of the other characteristic thus yields, for the characteristics l_+ and l_-, the following expressions:

$$\chi_+ \equiv \frac{1}{\rho V^2}\frac{\partial p}{\partial l_-} = \frac{\cos\mu}{\rho V^2}\frac{\partial p}{\partial s} - \frac{\sin\mu}{\rho V^2}\frac{\partial p}{\partial n}, \quad \chi_- \equiv \frac{1}{\rho V^2}\frac{\partial p}{\partial l_+} = \frac{\cos\mu}{\rho V^2}\frac{\partial p}{\partial s} + \frac{\sin\mu}{\rho V^2}\frac{\partial p}{\partial n}. \tag{7}$$

Here, χ is taken as positive for a compressive characteristic and negative for an expansive one. Using the Euler equation for the cross-stream (n-) momentum,

$$\rho V^2\frac{\partial\delta}{\delta s} + \frac{\partial p}{\partial n} = 0, \tag{8}$$

it follows that the characteristic strengths are given in terms of the local pressure gradient and streamline curvature by

$$\chi_+ = \frac{1}{M}[\sqrt{M^2-1}P + D], \quad \chi_- = \frac{1}{M}[\sqrt{M^2-1}P - D], \tag{9}$$

where P is the nondimensional pressure gradient in the flow direction and D is the streamline curvature, as defined in Eq. (2). Equation (9) indicates that the strength of the characteristics depends on both of the two quantities. Based on this foundation, we perform an in-depth analysis of the flow near the throat to investigate the underlying conditions for its formation, as illustrated in Fig. 13. Typically, as a result of the converging-diverging flow accelerating from subsonic to supersonic beneath the slip line, the pressure gradient P along it remains negative.

Meanwhile, the streamline curvature D is positive at the sonic throat Q, as this point marks the minimum of the slip line. It then follows from Eq. (9) that the strength χ_+ of the left-running characteristic l_+ can be either positive or negative, meaning it can be either a compression or an

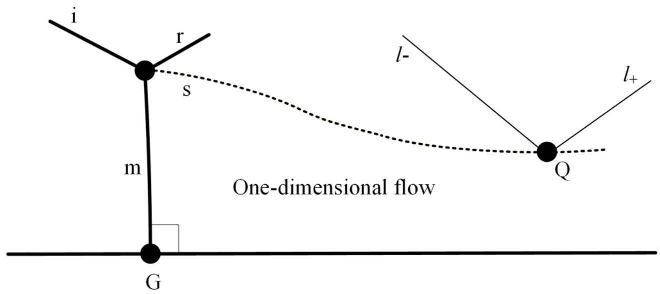

FIG. 13. Schematic illustration of the characteristics at the sonic throat Q on the slip line.

expansion wave. In contrast, the strength χ_- of the right-running characteristic l_- must be negative, indicating it is necessarily an expansion wave.

In fact, for the slip line to deflect toward a horizontal alignment, it must maintain a positive curvature over a finite distance upstream of the throat. This condition implies that the formation of a sonic throat necessitates the presence of a sustained expansion wave field. Therefore, sonic throats tend to emerge under the influence of the expansion fan at the trailing edge, which generates an exceedingly powerful negative pressure gradient that can rapidly deflect the slip line upward. Therefore, the formation of a throat in axisymmetric flow, independent of the expansion fan, must be related to the pressure gradient above the slip line. To eliminate the influence of the isentropic waves generated by the deflection of the slip line, an RR case is numerically simulated under conditions of $M_0 = 6$, $\delta_w = 10.7^\circ$, $R_c/R_0 = 0.1$, $R_e/R_0 = 0.5$. As illustrated in Fig. 14, the incident shock is reflected regularly over the center body, thereby creating a reflected shock. Since the surface of the center body is linear and does not generate any perturbations, the pressure variation behind the reflected shock is determined primarily by the upstream flow field. In the reflection of an oblique shock in planar flows, the pressure downstream of the reflected shock will remain uniform before the flow encounters the trailing edge expansion fan. However, Fig. 14 shows a decreasing pressure behind the reflected shock, implying the spontaneous generation of expansion waves. While the precise origin and conditions for these waves remain unclear due to the complexity of axisymmetric flows, this observation offers theoretical support for the existence of a sonic throat formation mechanism that does not rely on the trailing-edge expansion fan.

Nevertheless, in actual MR configurations, the slip line is inclined toward the axis of symmetry, resulting in circumferential compression, i.e., a reduction of the streamtube cross-sectional area because the circumference decreases as the flow moves inward. To evaluate the effect of this effect, pressure downstream of the reflected shock was calculated using the MOCC for a cone-tail model shown in Fig. 15. In this cone-tail model, the slip line is assumed to be a straight line in the meridional plane, coinciding with the cone generatrix. This deliberate simplification avoids

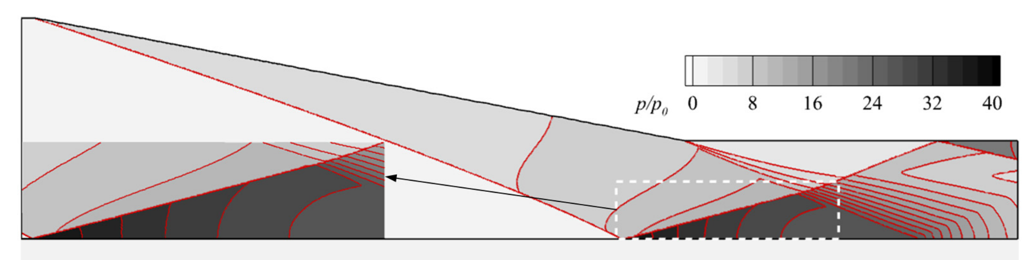

FIG. 14. Numerical pressure contours for an RR flow field over the surface of the center body under condition of $M_0 = 6$, $\delta_w = 10.7^\circ$, $R_c/R_0 = 0.1$, and $R_e/R_0 = 0.5$.

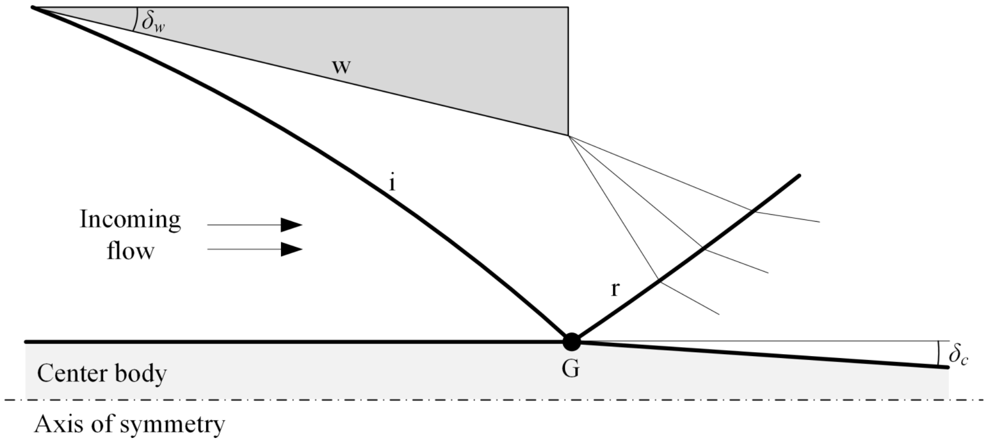

FIG. 15. Schematic illustration of the analytical model used to calculate the pressure distributions behind the reflected shock.

wave-generating deflection (unlike a curved slip line), thereby isolating the effect of slip-line inclination on the pressure distribution without the complication of curvature-induced waves. Given that the intensity of circumferential compression is contingent upon the direction of the flow, the center body is designed to deflect at the reflection point G, inclined toward the axis with an angle δ_c. Figure 16 provides the analytical pressure distributions along the surface of the center body before it reaches the expansion fan or the axis of symmetry for different inclination angles δ_c. It is evident that the inclination angle has a significant impact on the pressure distribution. When the inclination angle is 0°, the surface of the central body is straight, which corresponds to the scenario shown in Fig. 14. The pressure on the center body shows an overall declining trend, with only slight increases at both ends. As δ_c decreases, the reflected shock weakens, resulting in a continuous decrease in the initial pressure behind it. As a result of the circumferential compression effect, there is a change in

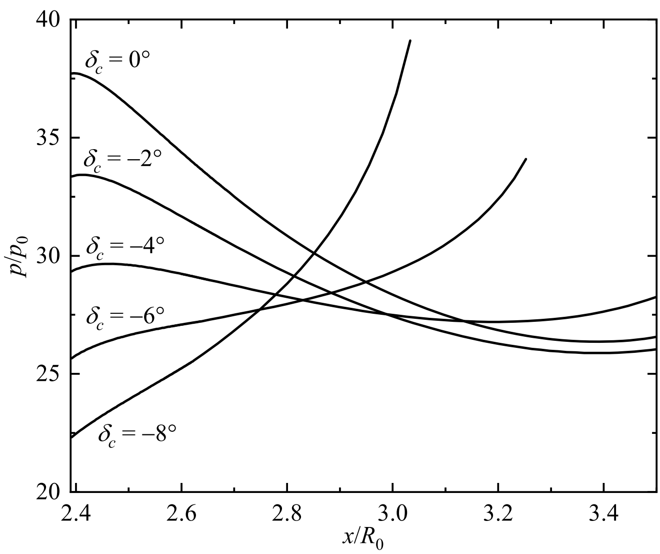

FIG. 16. Pressure distributions behind the reflected shock along the surface of the center body for different inclination angles δ_c under the condition $M_0 = 6$, $\delta_w = 10.7°$, $R_e/R_0 = 0.5$, and $R_c/R_0 = 0.1$.

the trend of pressure variation along the flow direction. As the inclination angle decreases to -2° and -4°, the rate of pressure decrease slows down, making it more challenging to form a throat. If the inclination angle continues to decrease to -6° and -8°, the circumferential compression (which intensifies as streamlines converge more sharply toward the axis, accelerating the flow-tube contraction) will continue to intensify and exceed the expansion effect from the upstream flow field. As a result, the pressure behind the reflected shock will no longer decrease but start to increase. Under these circumstances, the sonic throat is impossible to form without the expansion fan. This explains why a sonic throat independent of the trailing edge expansion fan has been observed only when the wedge angle is sufficiently small. At such angles, the triple point is very close to the von Neumann criterion, which can be seen in Fig. 10(a). This results in a small-sized Mach disk and a slight inclination angle of the slip line, leading to relatively weak circumferential compression.

The numerical simulations depicted in Fig. 17 further support the analysis presented above. The variations in the position of the supersonic throat with an increase in the center body radius are shown under conditions of $M_0 = 6$, $\delta_w = 12^\circ$, and $R_e/R_0 = 0.5$. The flow field is displayed using density gradient contours, to provide a clear visualization of the area affected by the expansion fan generated from the trailing edge. The red curve represents the sonic line, while the blue curve illustrates the direction of the right-running characteristic line (l-) at the sonic throat. In Fig. 17(a), the supersonic throat is observed to be situated within the influence range of the expansion fan when the center body radius is set to 0. The right-running characteristic line at the throat points toward the trailing edge, indicating that the formation of the sonic throat depends on the effect of the trailing edge expansion fan. With an increase in center body radius, a noticeable reduction in the size of the Mach disk and a smoother slip line is evident, indicating a diminishing effect of circumferential compression. Correspondingly, the formation of the sonic throat becomes more accessible and its location shifts upstream. When the center body radius reaches $0.06R_0$ [Fig. 17(b)], the sonic throat is outside the influence region of the expansion fan. At this point, the emitted characteristic line from the throat intersects with the wedge surface. Downstream of the sonic throat, another subsonic pocket is formed within the expansion fan's influence area due to the slip line's fluctuation. However, at this point, the sonic throat is isolated from the subsonic pocket by a supersonic region. Therefore, the expansion fan no longer impacts the formation of the sonic throat. In Fig. 17(c), a more prominent upstream movement of the sonic throat is observed with a further increase in the center body radius to $0.08R_0$. Downstream of the sonic throat, more subsonic pockets appear, alternating with supersonic regions.

IV. CONCLUSION

This paper establishes an analytical model to study the flow characteristics for axisymmetric internal shock MRs in steady supersonic flows. The proposed model is modified from the planar model for curved shock MRs by Zhang *et al.* [19] to account for the new features of axisymmetric internal flow. As the unique geometry component in axisymmetric internal flow, the presence of a center body has been included in the model. The use of the CST and MOCC in this model enables efficient prediction of flow structures, while simultaneously providing gradient information for the flow field, such as shock curvatures. When considering the overall configurations of the flow field, the analytical model demonstrates good agreement with numerical simulations, including the incident and reflected shocks, the Mach disk, and the slip line.

The flow characteristics of axisymmetric internal MRs are investigated using a combination of analytical and numerical studies. A parameter analysis of the Mach-disk size via various free stream and geometric conditions is conducted. It is suggested that, for small wedge angles, the triple point is close to the point corresponding to the von Neumann criterion, indicating the feasibility of using the criterion to estimate the size of the Mach disk in such cases.

The investigation into the shape of the slip line demonstrates that the sonic throat can be formed without the influence of the expansion fan generated by the wedge's trailing edge. In such cases, the radius of the Mach disk is unaffected by the outlet radius. Analysis indicates that the independent

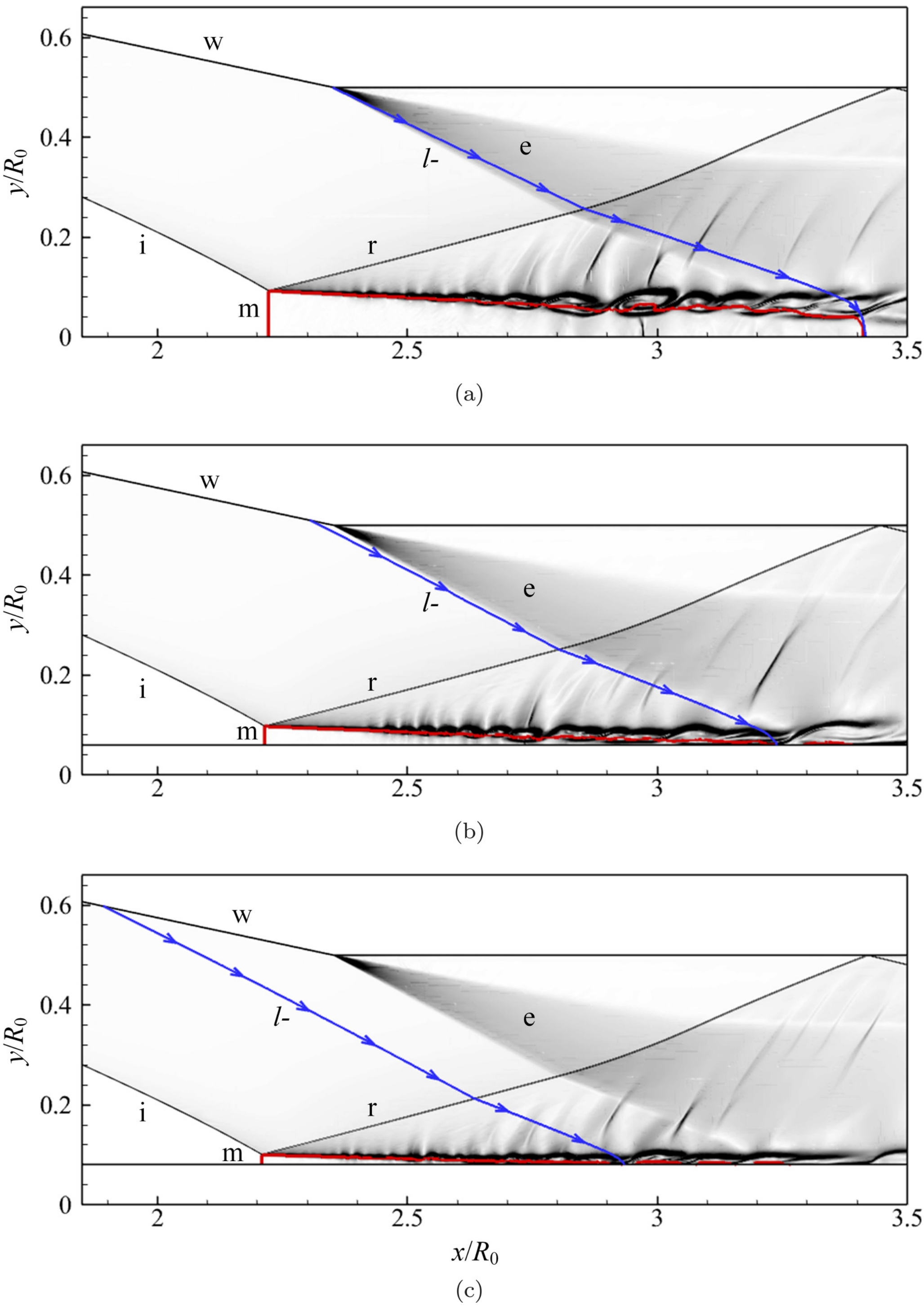

FIG. 17. Variations of the sonic throat position with the increase of the center body radius R_c under conditions $M_0 = 6$, $\delta_w = 12^\circ$, and $R_e/R_0 = 0.5$: (a) $R_c/R_0 = 0$; (b) $R_c/R_0 = 0.05$; and (c) $R_c/R_0 = 0.08$.

formation of the sonic throat is attributed to the negative pressure gradient that arises behind the reflection shock in axisymmetric internal flows. The pressure gradient is related to the slope of the slip line. A slip line that deflects from a downward inclination toward a flatter orientation is associated with a weaker circumferential compression effect, which allows the negative pressure gradient generated by upstream expansion waves following the reflected shock to become more dominant. This explains why the sonic throat independent of the expansion fan is feasible only in cases with sufficiently small wedge angles because the deflection of the slip line is slight under such conditions. The simulation results support this conclusion, showing that the sonic throat moves upstream and leaves the influence region of the expansion fan as the center body increases in size.

ACKNOWLEDGMENT

We acknowledge the support of the National Natural Science Foundation of China (NSFC, Grants No. 123B2037, No. 12302389, and No. 12372295).

DATA AVAILABILITY

The data that support the findings of this article are not publicly available upon publication because it is not technically feasible and/or the cost of preparing, depositing, and hosting the data would be prohibitive within the terms of this research project. The data are available from the authors upon reasonable request.

---

[1] E. Mach, Über den Verlauf von Funkenwellen in der Ebene und im Raume, Sitzungsber. d. Akad. Wiss. Wien **78**, 819 (1878).

[2] G. Ben-Dor, *Shock Wave Reflection Phenomena* (Springer Verlag, Berlin, 2007).

[3] J. von Neumann, Oblique reflection of shock waves, *John von Neumann Collected Works* (Pergamon Press, Oxford, UK, 1943).

[4] J. von Neumann, Refraction, intersection and reflection of shock waves, *John von Neumann Collected Works* (Pergamon Press, Oxford, UK, 1945).

[5] H. G. Hornung, H. Oertel, and R. J. Sandeman, Transition to Mach reflection of shock waves in steady and pseudo-steady flows with and without relaxation, J. Fluid Mech. **90**, 541 (1979).

[6] M. S. Ivanov, S. F. Gimelshein, and A. E. Beylich, Hysteresis effect in stationary reflection of shock waves, Phys. Fluids **7**, 685 (1995).

[7] G. Ben-dor, T. Elperin, and E. I. Vasiliev, Flow Mach number induced hysteresis phenomena in the interaction of conical shock waves—A numerical investigation, J. Fluid Mech. **496**, 335 (2003).

[8] M. S. Ivanov, A. N. Kudryavtsev, and D. V. Khotyanovskii, Numerical simulation of the transition between the regular and Mach reflection of shock waves under the action of local perturbations, Dokl. Phys. **45**, 353 (2000).

[9] A. N. Kudryavtsev, D. V. Khotyanovsky, M. S. Ivanov, and D. Vandromme, Numerical investigations of transition between regular and Mach reflections caused by free-stream disturbances, Shock Waves **12**, 157 (2002).

[10] C. A. Mouton and H. G. Hornung, Experiments on the mechanism of inducing transition between regular and Mach reflection, Phys. Fluids **20**, 126103 (2008).

[11] D. J. Azevedo, Analytical prediction of shock patterns in a high-speed wedge bounded duct, Ph.D. thesis, Department of Mechanical and Aeronautical Engineering, State University, Buffalo, NY, 1989.

[12] D. J. Azevedo and C. S. Liu, Engineering approach to the prediction of shock patterns in bounded high-speed flows, AIAA J. **31**, 83 (1993).

[13] H. Li and G. Ben-Dor, A parametric study of Mach reflection in steady flows, J. Fluid Mech. **341**, 101 (1997).

[14] C. A. Mouton and H. G. Hornung, Mach stem height and growth rate predictions, AIAA J. **45**, 1977 (2007).

[15] B. Gao and Z. N. Wu, A study of the flow structure for Mach reflection in steady supersonic flow, J. Fluid Mech. **656**, 29 (2010).

[16] C. Y. Bai and Z. N. Wu, Size and shape of shock waves and slipline for Mach reflection in steady flow, J. Fluid Mech. **818**, 116 (2017).

[17] S. Roy and R. Gopalapillai, An analytical model for asymmetric Mach reflection configuration in steady flows, J. Fluid Mech. **863**, 242 (2019).

[18] X. K. Guan, C. Bai, J. Lin, and Z. Wu, Mach reflection promoted by an upstream shock wave, J. Fluid Mech. **903**, A44 (2020).

[19] T. Zhang, K. J. Xu, C. G. Shi, C. X. Zhu, and Y. C. You, Reflection and transition of planar curved shock waves, J. Fluid Mech. **959**, A11 (2023).

[20] C. Y. Bai, Reflection of a centred compression wave, J. Fluid Mech. **984**, R3 (2024).

[21] A. A. Filippi and B. W. Skews, Supersonic flow fields resulting from axisymmetric internal surface curvature, J. Fluid Mech. **831**, 271 (2017).

[22] J. R. Cheng, T. Zhang, C. G. Shi, X. Y. Da, C. Zhu, and Y. You, Analytical reconstruction of axisymmetric curved shock wave/boundary layer interactions, Phys. Fluids **36**, 046125 (2024).

[23] Y. C. You, An overview of the advantages and concerns of hypersonic inward turning inlets, in *Proceedings of the AIAA International Space Planes & Hypersonic Systems & Technologies Conference* (AIAA, Reston, VA, 2011), pp. 2011–2269.

[24] Z. J. Cai, W. E. Hu, Z. C. Hu, C. G. Shi, X. G. Zheng, C. X. Zhu, and Y. C. You, The inverse design and three-dimensional analysis of double design points basic flow field based on wide range capture ability, Aerosp. Sci. Technol. **159**, 109964 (2025).

[25] S. Mölder, A. Gulamhussein, E. Timofeev, and P. Voinovich, Focusing of conical shocks at the center-line of symmetry, in *Shock Waves*, edited by A. F. P. Houwing and A. Paull (Panther Publishing and Printing, Canberra, 1997), pp. 875–880.

[26] H. G. Hornung, Oblique shock reflection from an axis of symmetry, J. Fluid Mech. **409**, 1 (2000).

[27] G. Shoev and H. Ogawa, Numerical study of viscous effects on centreline shock reflection in axisymmetric flow, Phys. Fluids. **31**, 026105 (2019).

[28] A. I. Rylov, On the impossibility of regular reflection of a steady-state shock wave from the axis of symmetry, J. Appl. Math. Mech. **54**, 201 (1990).

[29] T. Zhang, W. E. Hu, X. Y. Da, C. G. Shi, C. X. Zhu, and Y. C. You, Fully appreciating the impossibility of shock wave regular reflection from the axis of symmetry in axisymmetric internal flows, Phys. Fluids **36**, 076110 (2024).

[30] J. Z. Ji, Z. F. Li, D. X. Si, T. Zhang, C. G. Shi, Y. C. You, and J. M. Yang, Formation and evolution of Mach disk in axisymmetric internal conical flow, Acta Aerodyn. Sin. **40**, 129 (2022).

[31] A. Ferri, Application of the method of characteristics to supersonic rotational flow, in NACA Rep. No. 841, National Advisory Committee for Aeronautics (1946).

[32] N. P. Isakova, A. N. Kraiko, K. S. Pyankov, and N. I. Tillyayeva, The amplification of weak shock waves in axisymmetric supersonic flow and their reflection from an axis of symmetry, J. Appl. Math. Mech. **76**, 451 (2012).

[33] B. Shoesmith and E. Timofeev, On hysteresis at axisymmetric curved shock reflection from an axial cylinder, in *Proceedings of the 31st International Symposium on Shock Waves 1* (Springer International Publishing, Berlin, 2019), pp. 879–885.

[34] B. Shoesmith and E. Timofeev, Modelling of Mach reflections in internal axisymmetric steady supersonic flow, Shock Waves **31**, 945 (2021).

[35] B. Shoesmith and E. Timofeev, Shock reflection from an axial cylinder in axisymmetric supersonic steady flow, Shock Waves **35**, 759 (2025).

[36] G. K. Batchelor, *An Introduction to Fluid Dynamics* (Cambridge University Press, Cambridge, UK, 2000).

[37] L. P. Ronald, *Incompressible Flow* (Wiley, New York, NY, 2005).

[38] S. Mölder, Curved shock theory, Shock Waves **26**, 337 (2016).

[39] C. G. Shi, C. X. Zhu, Y. C. You, and G. S. Zhu, Method of curved-shock characteristics with application to inverse design of supersonic flowfields, J. Fluid Mech. **920**, A36 (2021).

[40] C. G. Shi, Y. C. You, X. G. Zheng, and C. X. Zhu, Analytical model for curved-shock Mach reflection, Phys. Fluids **35**, 031702 (2023).

[41] http://www.vtf.website.

[42] R. Deiterding, Block-structured adaptive mesh refinement—Theory, implementation and application, in *ESAIM Proceedings* (EDP Sciences, Les Ulis, France, 2011), Vol. 34, pp. 97–150.

[43] S. Laurence and R. Deiterding, Shock-wave surfing, J. Fluid Mech. **676**, 396 (2011).

[44] R. Deiterding, Parallel adaptive simulation of multi-dimensional detonation structures, Ph.D. thesis, Brandenburgische Technische Universität Cottbus, 2003.